Quantitative Comparison of Integral and Fractional Slot Permanent Magnet Vernier Motors

Liang Xu, *Student Member, IEEE*, Guohai Liu, *Member, IEEE*, Wenxiang Zhao, *Senior Member, IEEE*, Jinghua Ji, Huawei Zhou, Wanxiang Zhao, and Tingting Jiang

***Abstract*—This paper presents and compares two permanent magnet vernier (PMV) motors with fractional slot concentrated windings (FSCWs) and integral slot distributed windings (ISDWs). The ISDW PMV motor is newly proposed and optimized for a fair comparison with the existing FSCW one. The equations of back electromotive force of both motors are investigated and derived showing that the ISDW PMV motor has the potential to obtain higher torque capability. Also, their electromagnetic performances, such as torque capability, fault tolerance, loss, and efficiency, are calculated and compared by using the finite-element analysis. Then, the maximum power strategy for PMV motors operating at high speed is presented. The simulated results show that both motors possess excellent flux weakening capability. Finally, the effectiveness of the theoretical analysis is verified by the finite-element analysis results and experiments on a prototype FSCW PMV motor.**

***Index Terms*—Flux weakening capability, fractional slot, integral slot, permanent magnet motor, vernier motor.**

I. Introduction

COMPARED with conventional permanent magnet motors, the direct-drive permanent magnet motors have a lot of advantages. With the absence of a reduction gear, the problems, such as backlash, friction loss, and maintenance can be eliminated. In addition, to some extent, the complexities and failure possibility of the system can be lowered; thus, enhancing reliability and efficiency [1]–[3]. The permanent magnet vernier (PMV) motors have been regarded as an excellent candidate used for direct-drive applications, because it can offer high torque at low speed. With the growing demand for the desirable direct-drive, the PMV motors have attracted increasingly attention and have been a hot topic in many fields, such as electrical vehicle, wave energy conversion, ship propulsion, railway traction, and wind power generation [4]–[7].

PMV motor was first proposed in 1995 by A. Ishizak. It made clear that the PMV motor can obtain high torque at low speed and the steady torque equation was derived in [8]. Then, Toba and Lipo presented comprehensive design considerations of surface PMV motor for pursuing torque maximizing [9]. After that various new PMV topologies have been proposed to further improve torque density. In [10] and [11], both the torque density and power factor of the PMV motors has been improved by employing spoke magnets. To save costly rare earth magnet and cut cost, new motors with less rare-earth permanent magnet material, weaker ferrite magnets, or no magnets has become good solutions [2], [12]–[15]. A PMV motor with ferrite has been proposed in [16], which reached the targeted torque for electrical vehicle and met the cost constraints. Also, a consequent pole PMV motor was proposed in [17] to alleviate flux leakage and reduce rare-earth magnet consuming.

Recently, it has been verified that fractional slot concentrated windings (FSCW) motors possess high power density, high efficiency, high fault tolerance, and low torque ripple [18]–[20], as well as reduction of the copper usage due to the short end turns. Considering these merits of the FSCW motors, a single-layer FSCW was adopted in a multiphase PMV motor for electrical vehicle applications in which the desirable fault-tolerant capability was improved [4]. An analysis of a PMV motor with FSCW also showed that the cogging torque and output torque ripple were insignificant [21]. In [22], the electromagnetic performances of six FSCW PMV motors with different slot per pole per phase value were compared. All of these studies confirm that the FSCW is also suitable for the PMV motor because the magnetic gearing effect is still working in these topologies. However, the comparison between PMV motors with FSCW and integral slot distributed windings (ISDW) is insufficient. It is well known that for the conventional FSCW and ISDW surface PM motors, their torque densities are close to each other when their PM pole-pairs number is identical. However, this conclusion is not suitable for PMV ones. This is because the harmonic component of PM, which is modulated by the flux modulation poles (FMPs), can produce a continuous torque except for the fundamental one in the conventional PM motor.

Apart from the high torque capability, high-speed operation is also an attractive feature in up-to-date applications, such as electric and hybrid traction. In [23], the comparisons between conventional PM synchronous and PMV motors showed that the PMV ones had better flux weakening capability. However, only the ISDW PMV motor was carried out and the corresponding FSCW one was not considered. In [24] and [25], flux weakening capability of a surface PM motor was significantly enhanced by employing the FSCW to replace the ISDW. It means that various winding layout have dramatic influence on the flux weakening

Manuscript received December 12, 2014; revised April 1, 2015; accepted May 8, 2015. This work was supported by the National Natural Science Foundation of China under Grant 61273154, Grant 51422702, and Grant 51477068; by the Natural Science Foundation of Jiangsu Province under Grant BK20130011; by the Graduate Education Innovation Project of Jiangsu Province under Grant KYLX-1049; and by the Priority Academic Program Development of Jiangsu Higher Education Institutions. Paper no. TEC-00837-2014. *(Corresponding author: Wenxiang Zhao.)*

The authors are with the School of Electrical and Information Engineering, Jiangsu University, Zhenjiang 212013, China (e-mail: 337263042@qq.com; ghliu@ujs.edu.cn; zwx@ujs.edu.cn; jjh@ujs.edu.cn; zhouhuawei@ujs.edu.cn; 15262901862@139.com; 1014111422@qq.com).

Color versions of one or more of the figures in this paper are available online at http://ieeexplore.ieee.org.

Digital Object Identifier 10.1109/TEC.2015.2434931

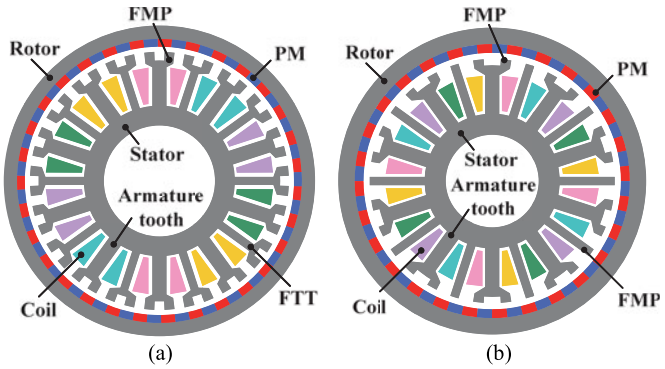

Fig. 1. Cross sections of PMV motors. (a) FSCW motor. (b) ISDW motor.

capability of PM motors. Hence, it is very essential to investigate and compare PMV motors with FSCW and ISDW, respectively, for the purpose of giving a comprehensive evaluation of flux weakening capability of the PMV motors.

The major objective of this paper is to evaluate and confirm the merits and demerits of the FSCW and ISDW PMV motors. In Section II, an ISDW PMV motor will be newly proposed and optimized for a fair comparison with the existing FSCW one. Their operation principles will be described in Section III in order to derive and analyze their no-load back electromotive forces (back-EMFs). In Section IV, the electromagnetic performances, such as torque capability, fault tolerance, loss and efficiency, of the two motors will be compared. In Section V, their flux weakening capability will be discussed and analyzed by using the presented flux weakening control strategy. The prototype motor and its experimental results will be shown in Section VI. Finally, the conclusions will be drawn in Section VII.

II. Topology and Features

The topology of the existing five-phase FSCW PMV motor in [4] is shown in Fig. 1(a). There are 20 slots in the stator and 62 poles in the rotor. Each stator tooth is split into two FMPs; thus, containing 40 FMPs totally. For the proposed ISDW counterpart, its stator also has 20 teeth and each tooth is split into two FMPs alternately; thus, containing 30 FMPs totally, which differs from the existing one. According to the magnetic gearing effect [8]–[11], the number of PM poles in the outer rotor of the ISDW motor can be set to 56, 58, and 62, which is similar to the existing one when the ISDW motor has 30 FMPs. Obviously, the 62 rotor poles ISDW PMV motor has the same rotor pole pairs as the existing FSCW one, but its winding pitch is very long as well as the 58 rotor poles ISDW one which significantly increases the end length of winding and results in high copper loss as compared to the existing FSCW PMV motor. Hence, taking the suitable winding layout and rotor pole number into consideration, the ISDW PMV motor with 56 rotor poles are chosen, and the newly proposed ISDW one is shown in Fig. 1(b). With the magnetic gearing principle, the number of armature winding pole pair of the existing FSCW and proposed ISDW motors can be calculated to be 9 and 2, respectively. Hence, it should be noticed that the number of armature winding pole pair and rotor pole pair of the both PMV motors are not identical, which is distinct from that of the conventional PM motors. It is essential to discuss the difference in designing PMV motors as compared to the conventional PM motors. The authors have designed and fabricated three kinds of conventional FSCW PM motors with high reliability in previous works, including surface PM type for coupling a magnetic gear, interior spoke PM type, and interior V-shaped PM type. They are designed with the same outer rotor radius, current density, and slot fill factor, and their detailed specifications can be found in [26]. For facilitating comparative study, the two PMV motors herein also designed with the same outer rotor radius, current density, and slot fill factor as the existing conventional PM motors. The effective magnetic loading of the PMV motors, as compared with these conventional PM motors, is low due to the existence of substantial useless space magnetic field harmonics. Therefore, the slot area and electrical loading design for the PMV motors should be reconsidered and enlarged to compensate the low magnetic loading. Hence, the both PMV motors in this paper should be designed with larger slot area and higher ampere turns than that of the conventional PM motors. The key design data are summarized in Table I. It can be seen that the both motors have the same air-gap length, outside rotor radius, stack length, and current density. Also, their grades of material of magnet, core, and armature winding are all the same. It should be noticed that only the final optimized design data of the FSCW motor are listed, while for the FSCW one, both of the initial and optimized

TABLE I
Comparison of Design Specifications

Item and symbol	FSCW PMV	Initial ISDW PMV	Optimized ISDW PMV
Phases, N_{ph}	5	5	5
Number of slots, S	20	20	20
Number of FMPs, Z_1	40	30	30
Number of rotor pole pairs, Z_2	31	28	28
Number of armature winding pole pairs, p	9	2	2
Outside stator radius, R_{so} (mm)	60	60	60
Inside stator radius, R_{si} (mm)	25	25	22
Outside rotor radius, R_{ro} (mm)	70	70	70
Inside rotor radius, R_{ri} (mm)	60.5	60.5	58.5
Air-gap radius, R_{δ} (mm)	60.25	60.25	58.25
Rotor yoke width, w_{ry} (mm)	6	6	9
Stack length, l_{stk} (mm)	60	60	60
Armature tooth width, w_{at} (mm)	6.6	6.6	6.7
Fault-tolerant tooth width, w_{ft} (mm)	3.8	–	–
FMP angle, β_{fmp} (degree)	4.5	6	4
PM thickness, h_{pm} (mm)	3.5	3.5	2.5
Air-gap length, δ (mm)	0.5	0.5	0.5
Per slot area, (mm^2)	168.9	139.6	166.8
Stator turns per coil, N_{tpc}	48	40	48
Series coils per phase, N_{scpp}	2	2	2
PM material	N35H	N35H	N35H
Remanence of PM, B_r, (T)	1.23 (20 °C)	1.23 (20 °C)	1.23 (20 °C)
Coercive force of PM, H_c, (kA/m)	890 (20 °C)	890 (20 °C)	890 (20 °C)
Iron lamination	50 WW465	50 WW465	50 WW465
Copper mass (kg)	1.09	1.84	2.21
Magnet mass (kg)	0.61	0.61	0.37
Iron mass (kg)	3.54	3.75	3.94
Total mass (kg)	5.24	6.2	6.52

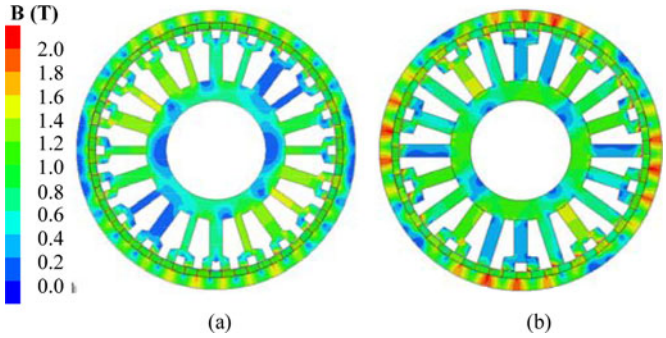

Fig. 2. Magnetic flux density of PMV motors at nominal current. (a) FSCW motor. (b) ISDW motor.

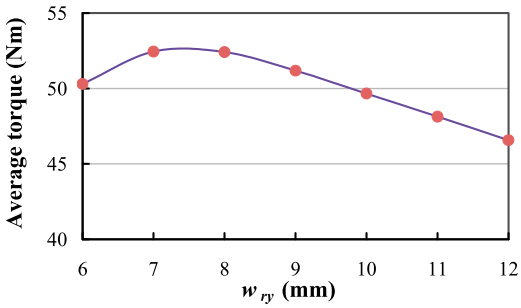

Fig. 3. Average torque versus the width of rotor yoke.

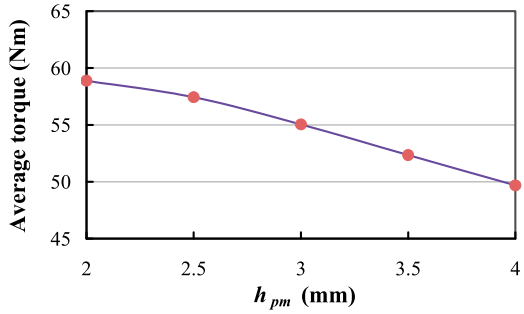

Fig. 4. Average torque versus the thickness of PM.

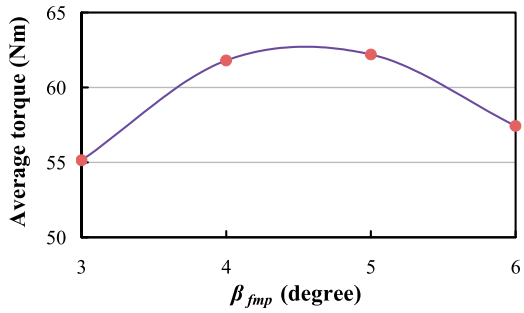

Fig. 5. Average torque versus the angle of FMP.

TABLE II
RESULTS OF THE INITIAL AND OPTIMIZED ISDW PMV MOTORS

Items	Initial	Optimized
Rotor speed (r/min)	600	600
Nominal current (A_{rms})	10	10
Nominal current density (A_{rms}/mm^2)	6.6	6.6
Nominal electrical loading (A_{rms}/cm)	105.7	131.1
PM flux linkage (m·Wb_{rms})	33.6	44.8
Fundamental amplitude of back-EMF (V)	82.6	111.5
Average torque (N·m)	44.0	61.8
Air-gap shear stress (psi)	4.95	6.95
Motor mass (kg)	6.2	6.52
Motor volume (L)	0.92	0.92
Average torque per motor mass (N·m/kg)	7.1	9.5
Average torque per motor volume (N·m/L)	47.8	67.2

data are listed, and its current density, slot fill factor, outer rotor radius, and stack length are fixed in the optimization procedure.

Two 2-D finite-element models of the two PMV motors are built based on the design parameter in Table I, respectively. Fig. 2 illustrates their magnetic flux density distributions at nominal current. It can be seen that the maximum flux density of the FSCW PMV motor is in the range from 1.4 to 1.6 T in the stator teeth and rotor yoke. However, for the ISDW PMV motor, the maximum flux density in the rotor yoke is over 2.0 T. It is obvious that compared with that of the FSCW PMV motor, the rotor yoke of the ISDW PMV one is liable to be saturated. This is due to the operation principle of PMV motor, which will be interpreted in the next section.

In order to alleviate the magnetic saturation in the rotor as shown in Fig. 2(b), the rotor yoke width of the ISDW PMV motor should be considered and increased at first. In addition, as revealed in [9] and [28], no-load back-EMF and output torque of the PMV motor are very sensitive to the PM thickness and the ratio of FMP tooth width to FMP pitch. Therefore, these key parameters are chosen to investigate and optimize the performance of the proposed ISDW PMV motor.

In Fig. 3, the effect of rotor yoke width on average torque is investigated. When w_{ry} varies from 6 to 7 mm, the output torque increases because saturation in the rotor yoke is alleviated. Contrarily, the output torque decreases with the increase of w_{ry} from 7 to 12 mm due to the reduced diameter of air gap. When considering a compromise between mitigating saturation and enlarging the length of air-gap diameter, w_{ry} is chosen to be 9 mm for the next optimization step. Fig. 4 shows the output torque versus PM thickness. It can be seen that the torque decreases from 58.9 to 49.7 N·m (a reduction of 15.6%) when h_{pm} increases from 2 to 4 mm. It means that a thin PM is more suitable for the PMV motor. However, a thin PM may be more likely to suffer from the irreversible demagnetization. Therefore, even though the output torque reaches the maximum value when h_{pm} is equal to 2 mm, $h_{pm} = 2.5$ mm is chosen. Fig. 5 shows that the average torque of a PMV motor is also affected by the angle of FMP, which is chosen to be 4°. The initial and optimized ISDW PMV motors are compared in Table II. The no-load back-EMF of the optimized motor has an increase of 35% than that of the initial one. It benefits from the larger slot area for coils and alleviative magnetic saturation in the rotor yoke. In addition, the torque density of the optimized motor also improved significantly.

After the optimization of the output torque of the ISDW PMV motor, it is very essential to check the irreversible demagnetization of the proposed ISDW and the existing FSCW motors

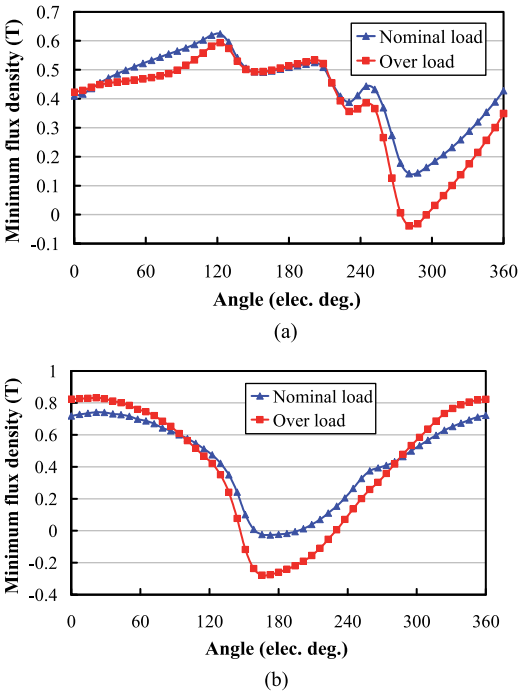

Fig. 6. Minimum flux densities versus rotor positions of both PMV motors. (a) FSCW motor. (b) ISDW motor.

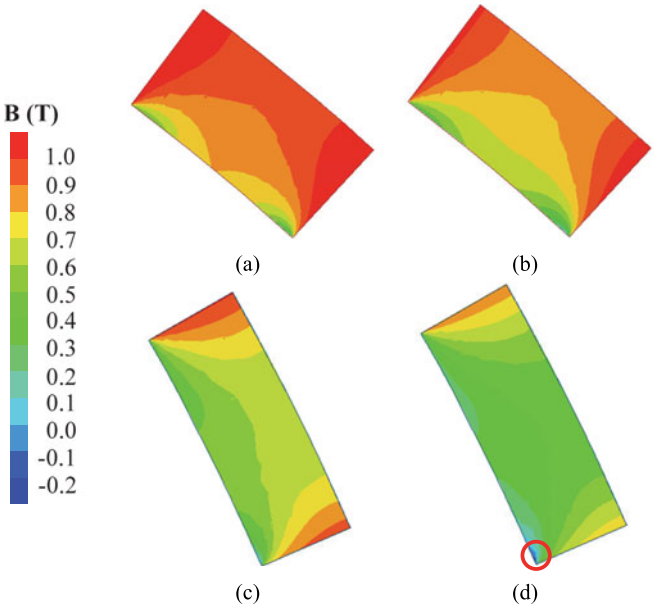

Fig. 7. Flux density distributions of PMs at the worst demagnetization of both PMV motors under nominal load and overload. (a) FSCW motor under nominal load. (b) FSCW motor under overload. (c) ISDW motor under nominal load. (d) ISDW motor under overload.

because the irreversible demagnetization can seriously influence their electromagnetic performances. To investigate the irreversible demagnetization of PMs, both motors are operated under nominal load and overload representing twice the nominal current density in this paper, and the temperature of PMs is held constant of 70 °C. Meanwhile, the critical flux density of irreversible demagnetization is assumed to be 0 T in the magnetization direction of PMs. Fig. 6(a) and (b) show the minimum normal flux density versus rotor positions of both motors under nominal load and overload, respectively. It can be seen that the FSCW motor exhibits superior capability of withstanding irreversible demagnetization as compared to ISDW motor, which is due to its thicker PMs. Obviously, partial irreversible demagnetization occurs in both motors when they operate under overload conditions. Fig. 7 illustrates the detailed flux density distributions in PMs of both motors at nominal and overloads to further observe the partial demagnetization region. As expected, the worst demagnetization occurs in the ISDW motor, which is marked in circle, when it operates at twofold overload. Also, it can be calculated that the demagnetization region only accounts for ~0.1% of the total PM region. Hence, the influence due to partial demagnetization in both motors is very slight which can be ignored, and the PMs of both motors are safe when they operate under nominal load and overload.

III. Operation Principle

It is well known that the operation principle of the PMV motor is based on the so-called magnetic gearing effect [8]–[11], [27], [28]. The low pole-pairs number of armature windings with high magnetic speed is modulated by the FMP to match the high pole-pairs number of PM with low magnetic speed. Thus, a small displacement of the rotor results in a significant change of the flux, which yields to a high torque. To utilize the magnetic gearing effect and maximize torque capability, the number of rotor pole-pairs Z_2, FMPs Z_1, and armature winding pole-pairs p should satisfy the following relationship:

$$Z_2 = Z_1 - p \tag{1}$$

$$Z_1 = 2aN_{\mathrm{ph}}qp \tag{2}$$

$$a = \frac{Z_1}{S} \tag{3}$$

where a and q are a positive number and the number of slot per pole per phase, respectively.

To identify the magnetic gearing effect in the PMV motor, its no-load back-EMF is developed and obtained by PM magnetomotive force F_{PM} and the magnetic permeance P due to the toothed FMP structure. F_{PM} and P of the PMV motor can be expressed as

$$F_{\mathrm{PM}}(\theta,\theta_m) \approx F_{\mathrm{PM1}}\cos Z_2(\theta-\theta_m) \tag{4}$$

$$P(\theta) \approx P_{s0} + P_{s1}\cos(Z_1\theta) \tag{5}$$

where θ and θ_m are the mechanical angle on the stator and the one on the rotor, respectively. Then, the air-gap flux density of PM modulated by FMPs can be obtained as

$$\begin{aligned} B(\theta,\theta_m) &\approx F_{\mathrm{PM}}(\theta,\theta_m)P(\theta) \\ &= B_{\mathrm{PM1}}\cos((Z_2+Z_1)\theta - Z_2\theta_m) + B_{\mathrm{PM0}}\cos Z_2(\theta-\theta_m) \\ &+ B_{\mathrm{PM1}}\cos((Z_2-Z_1)\theta - Z_2\theta_m) \end{aligned} \tag{6}$$

where $B_{\mathrm{PM0}} = F_{\mathrm{PM1}}P_{s0}$ and $B_{\mathrm{PM1}} = \frac{F_{\mathrm{PM1}}P_{s1}}{2}$.

From (6), it can be seen that air-gap flux density in the PMV motor consists of three components. The second term represents

the flux density only produced by PM, in which the modulation effect on the PM magnetic field can be neglected. Hence, the second term can be regarded as the component like the conventional motor [8]. The first and third terms are produced based on the modulation effect between PMs and FMPs. The first term represents a short wavelength of rotational magnetic field with a high pole-pairs number; thus, the back-EMF induced by this component is insignificant. For the third term, since its pole-pairs number of the rotational magnetic field is the same as the fundamental component of the armature windings, much more considerable back-EMF than the one in the first term can be obtained. Therefore, B_{PM1} is generally referred to as the fundamental component of flux density in the PMV motor [8], [9]. Also, it is termed as an additional prominent component, which is unique one produced by the magnetic gearing effect in the PMV structure [9]. For the conventional PM motor, there exist no other harmonic components to produce useful back-EMF, except for the fundamental component. This is due to the constraint that the pole-pairs number of the armature windings and PMs must be identical. However, in the PMV motor, the pole-pairs numbers of armature windings and PMs are not identical. Both the fundamental and harmonic components of the flux density can be effectively utilized so that higher back-EMF and higher torque density can be achieved. Considering both components of the air-gap flux densities, the phase back-EMF of the PMV motor can be expressed as

$$\begin{aligned} E_{\mathrm{ph}} &= E_{\mathrm{PM0}} + E_{\mathrm{PM1}} \\ &= K_{w0} N_{\mathrm{tpc}} N_{\mathrm{scpp}} D_g l_{\mathrm{stk}} \omega_m B_{\mathrm{PM0}} \\ &\quad + K_{w1} N_{\mathrm{tpc}} N_{\mathrm{scpp}} D_g l_{\mathrm{stk}} \omega_m \frac{Z_2}{p} B_{\mathrm{PM1}} \end{aligned} \tag{7}$$

where ω_m is the mechanical angular velocity, D_g is the air-gap diameter, and K_{w0} and K_{w1} are the harmonic and fundamental components winding factor.

By substituting (1) and (2) into (7), the phase back-EMF of PMV motor E_{ph} becomes

$$\begin{aligned} E_{\mathrm{ph}} &= K_{w0} N_{\mathrm{tpc}} N_{\mathrm{scpp}} D_g l_{\mathrm{stk}} \omega_m B_{\mathrm{PM0}} \\ &\quad + K_{w1} N_{\mathrm{tpc}} N_{\mathrm{scpp}} D_g l_{\mathrm{stk}} \omega_m G_r B_{\mathrm{PM1}} \end{aligned} \tag{8}$$

$$G_r = 2aN_{\mathrm{ph}}q - 1. \tag{9}$$

In the PMV motor, the amplitude of the B_{PM1} is less than the B_{PM0}, whereas the B_{PM1} provides main back-EMF due to the magnetic gearing effect. However, it is very hard to enhance the B_{PM1} to reach the amplitude of B_{PM0}. Thus, selecting a higher G_r, namely magnetic gear ratio is an effective way to enhance the amplitude of back-EMF. Further observation from (9) reveals that a higher slots per pole per phase value q is appropriate to obtain high back-EMF. It is worthwhile to note that K_{w1} can significantly affect the back-EMF of the harmonic component as well as the value of q. Therefore, the design of winding layout for the PMV motor is very essential. Although the rotor PM and armature winding pole-pairs number are not identical, the winding connection also can be described and analyzed by the star of slots like the conventional PM motors.

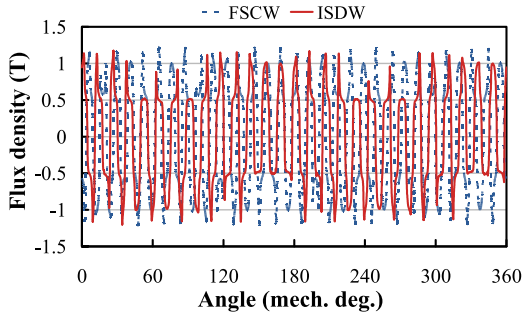

Fig. 8. No-load air-gap flux density versus the rotor position.

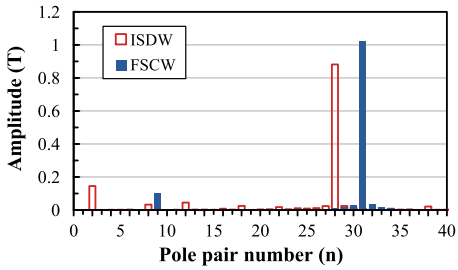

Fig. 9. Space harmonic spectrum of no-load air-gap flux density of the both motors.

IV. Performance Analysis

In this section, two five-phase PMV motors with FSCW and ISDW will be quantitatively analyzed and compared at the PM temperature of 20 °C by means of the time-stepping finite-element method. Their key dimensions and specifications are listed in Table I.

A. Back-EMF and Torque

The air-gap flux density waveforms of the two motors only due to PM are shown in Fig. 8. It can be seen that both motors have similar level of magnetic loading. The maximum flux density of the FSCW and ISDW are 1.22 and 1.17 T, respectively. Fig. 9 shows their corresponding space harmonic spectrum. Obviously, the 9 pole pairs cannot exist in a conventional PM motor with 31 PM pole pairs. However, for the FSCW motor, the useful harmonic flux density of 9 pole pairs is obtained by using the flux modulation as well as the 2 pole pairs for the ISDW one with 28 PM pole pairs. The flux densities of 9 and 31 pole pairs in the FSCW motors are up to 0.098 and 1.022 T, respectively. Then, their appropriate winding connections and winding factors can be easily obtained by using the method of star of slots. Fig. 10(a) and (b) illustrates the star of slots of the fundamental and harmonic component of the FSCW motor. In order to facilitate to show direction of the conductor, the positive and negative directions of conductor in one slot are marked as solid and dotted lines, respectively. To maximize the winding factor of the fundamental component, the phasor 1, −2, −11, 12 are connected together for constituting one phase. Then, the winding layout also would be used for the harmonic component as shown in Fig. 10(b). Since the two components have the same star of slots, their winding factor is identical with the value of

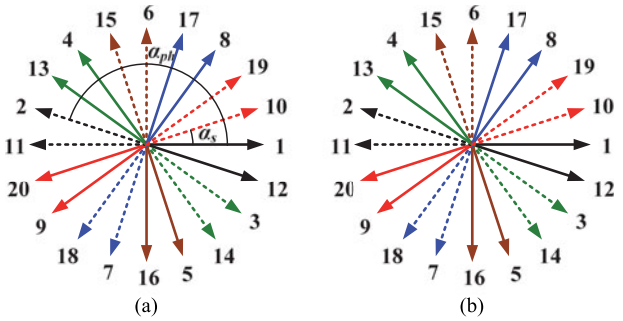

Fig. 10. Star of slots of the FSCW motor. (a) Fundamental component. (b) Harmonic component.

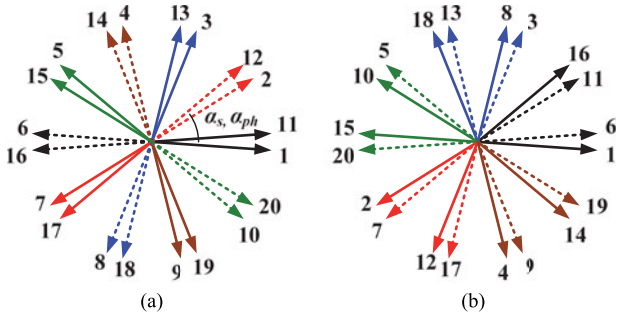

Fig. 11. Star of slots of the ISDW motor. (a) Fundamental component. (b) Harmonic component.

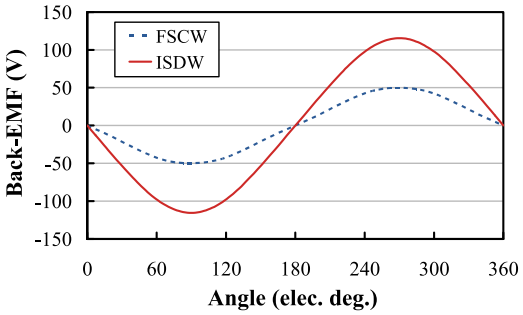

Fig. 12. No-load back-EMF waveforms of PMV motors.

cos9° (0.988). The star of slots of the ISDW motor is shown in Fig. 11(a) and (b). The winding factor of the fundamental component one is unity which is well-known advantage of the ISDW. However, it is quite remarkable that the winding factor of the harmonic component is zero. Thus, it can not contribute to a useful induced voltage although the harmonic flux density in the air gap is very prominent.

The no-load back-EMF waveforms of the two motors at nominal speed of 600 r/min are shown in Fig. 12. Both of them are very sinusoidal due to the inherent merit of the PMV motor. It can be seen that the back-EMF amplitude of the both motors are significantly higher than the conventional PM motor, revealing that both of them can offer higher torque [4]. In addition, it should be noticed that the back-EMF of the ISDW PMV motor is twice that of the FSCW one. Compared with the FSCW PMV

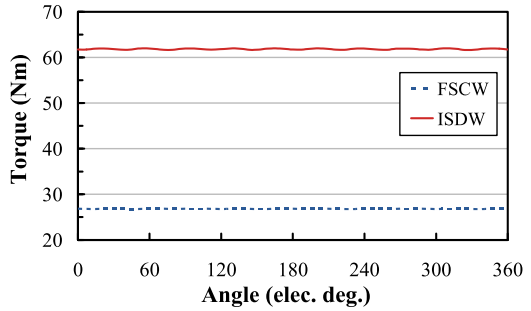

Fig. 13. Comparison of torque capability of PMV motors.

motor with the slots per pole per phase value of 2/9, the ISDW PMV motor has a unity value, which means that the ISDW one possesses higher value of G_r. It can be calculated that the G_r of the ISDW motor is 14, which is more than four times that of FSCW one with 31/9; thereby, achieving stronger magnetic gearing effect and higher back EMF. Due to their sinusoidal and symmetrical back-EMFs, both motors are suitable for brushless ac operation. By using $i_d = 0$ control and applying nominal current into the five-phase windings, the output torque waveforms versus rotor positions of the two motors are obtained as shown in Fig. 13. It can be seen that the torque ripple of the two motors are insignificant, which benefit from the sinusoidal back-EMF and low cogging toque. The ISDW motor exhibits a significant advantage over the FSCW one in terms of torque capability at fixed motor volume, magnetic loading, electrical loading, and similar PM pole-pairs number. Therefore, it implies that higher value of slots per pole per phase has more potential in obtaining higher torque for either ISDW or FSCW PMV motors on the condition of similar numbers of PM pole pairs and slots. This conclusion can be used as an effective and necessary supplementation for the relationship between FSCW and ISDW motors [28].

B. Loss and Efficiency

Apart from the aforementioned performance of no-load back-EMF and output torque, loss and efficiency are also important characteristics of the PM motor. This section will compare and analyze the loss and efficiency of the two motors at nominal operating conditions.

To calculate the copper loss of the motors, the total length of armature windings should be determined at first. A simplified winding model, in which end-turns winding are assumed to be semicircular, is used to calculate the total winding lengths. The copper loss p_{cu} of the two motors can be express as follows:

$$p_{\mathrm{cu}} = \frac{I_a^2 \rho_{\mathrm{cu}} (l_{\mathrm{stk}} + l_{\mathrm{end}}) N_{\mathrm{tpc}} S}{A_{\mathrm{cond}}} \tag{10}$$

where I_a is the rms armature current, ρ_{cu} is the electrical resistivity of copper, l_{end} is the average armature end-winding lengths, and A_{cond} is the area of per conductor.

The iron core loss and PM loss are evaluated by the finite-element analysis. Fig. 14 compares the loss of the two motors at the nominal speed of 600 r/min and nominal current of 10 A_{rms}, including copper loss, iron core loss, and eddy loss in

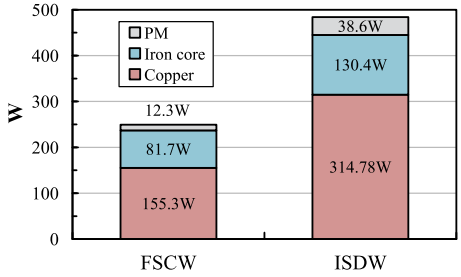

Fig. 14. Loss detail at nominal operating conditions.

magnet. It can be observed that the copper loss and iron core loss are dominant in the total loss of the two motors, while the PM loss comprises only a small part of their total loss (4.9% of the FSCW and 8.1% of the ISDW). In the case of copper loss, the FSCW motor has an overwhelming advantage, which is only half of the ISDW one. This is because the FSCW one adopts concentrated windings, which significantly reduce the end length of windings. Neglecting the friction and windage loss and stray loss, the efficiency of the two motors can be expressed as follows:

$$\eta = \frac{T_{\rm out}\omega_m}{T_{\rm out}\omega_m + p_{\rm cu} + p_{\rm iron} + p_{\rm pm}} \tag{11}$$

where $T_{\rm out}$ and ω_m are the average output torque and mechanical angular velocity of the two motors, respectively, and $p_{\rm cu}$, $p_{\rm iron}$, and $p_{\rm pm}$ are copper loss, iron core loss, and PM loss, respectively. The efficiency of the ISDW motor is 88.9%, which is slightly higher than the FSCW one of 87.1%.

V. Flux Weakening Capability

In order to investigate and predict the flux weakening capability of PMV motors, the characteristic current $I_{\rm ch}$ should be calculated in the first place, defined as

$$I_{\rm ch} = \frac{\lambda_m}{L_d} \tag{12}$$

where λ_m and L_d are the rms magnet flux linkage and d-axis inductance, respectively. The optimal flux weakening region can be achieved when the $I_{\rm ch}$ is equal to the nominal current I_r [24]. For the conventional surface PM motor, $I_{\rm ch}$ is much larger than I_r because the surface mounted magnets increase the effective air-gap length and lower the inductance. While in case of the PMV motor, it inherently has large inductances and generally overtakes the magnet flux linkage; thus, inevitably leading to poor power factor. In addition, it is worth to mention that the large inductance also reduces $I_{\rm ch}$ even smaller than I_r [28]. Important parameters with respect to the flux weakening capability of the two motors, including the nominal and characteristic current values, are calculated and listed in Table III. Obviously, the values of $I_{\rm ch}$ are about half the values of I_r in the two motors. It means that both motors can be fully weakened theoretically [29].

A maximum power control strategy at the flux weakening operation region for the PMV motors herein will be proposed and presented. The average output torque and output power of

TABLE III
Current and Inductance Parameters

Items	FSCW	ISDW
Magent rms flux linkage (Wb)	0.0171	0.0448
D-axis inductance (mH)	3.15	10.30
Characteristic rms current (A)	5.43	4.35
Nominal rms current (A)	10	10

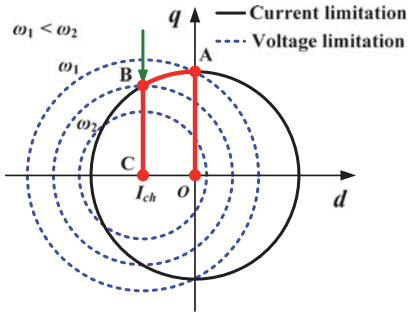

Fig. 15. Current strategy for maximum power under limited voltage and current amplitudes.

the two motors are expressed as follows:

$$T_{\rm out} = 5Z_2[\lambda_m i_q + (L_d - L_q) i_d i_q] \tag{13}$$

$$P_{\rm out} = T\omega_m = 5\omega_m Z_2[\lambda_m i_q + (L_d - L_q) i_d i_q] \tag{14}$$

where L_d and L_q are the d-axis and q-axis inductances, respectively, and i_d and i_q are the d-axis and q-axis currents, respectively.

The optimal current vector for maximum power under limited voltage and current amplitudes are shown in Fig. 15. At low-speed region (region I), both motors operate under the maximum torque per ampere (MTPA) control along the red straight line OA from origin point to point A. The point A shown in Figs. 15–Fig. 17(a) represents the both motors operate at the corner speed of 600 r/min and nominal rms current of 10 A. Meanwhile, the terminal voltages of the both motors reach their limits, and are noted as $u_{\rm lim}$. Then, the speed of the two motors cannot continue to increase due to the limited capacity of inverter. In order to widen the speed range, the phase angle of current angle has to lead q-axis to produce a demagnetization current i_d; thus, ensuring the terminal voltage not to beyond its limit. The flux weakening region herein is termed as region II. In this region, the current vector goes along with the red arc AB from point A to point B as shown in Fig. 15. Figs. 16(b) and 17(b) show the output power of the two motor. Obviously, it can be seen that from the point A to point B (region II), the output power is going up. After reaching the point B, the maximum power control is adopted for the next flux weakening region (region III). The current vector is drawn in red straight line BC from point B to point C as shown in Fig. 15. In this region, the current amplitude reduces, while the terminal voltage keeps its limit. Also, there exist the following rules:

$$u_{\rm lim} = \omega_e \sqrt{(L_q i_q)^2 + (L_d i_d + \lambda_m)^2} \tag{15}$$

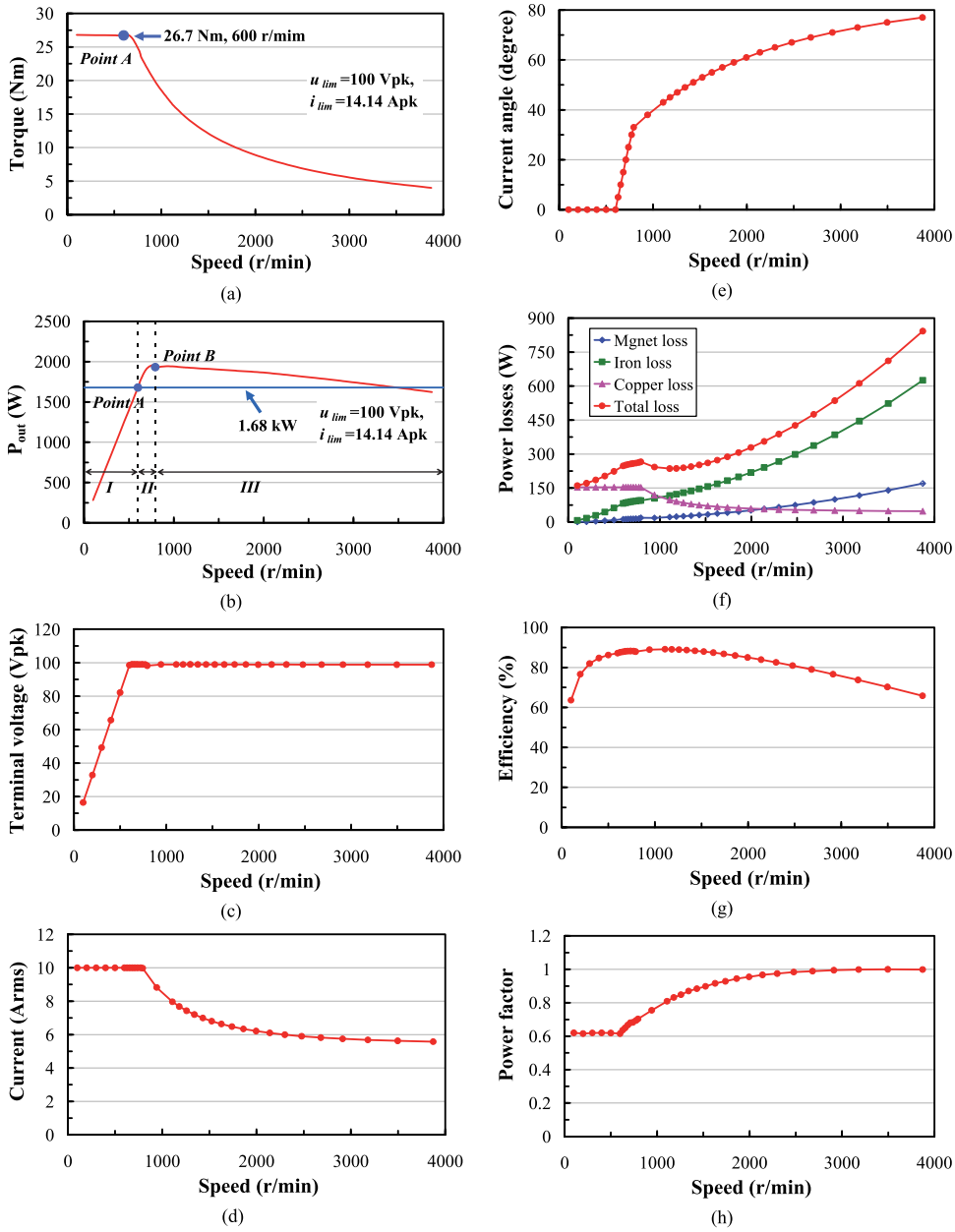

Fig. 16. Calculated output versus speed envelope for the FSCW motor. (a) Torque. (b) Output power. (c) Terminal voltage. (d) Current. (e) Current angle. (f) Power losses. (g) Efficiency. (h) Power factor.

$$\frac{dP_{\text{out}}}{di_d} = 0. \tag{16}$$

Substituting (14) into (16) and satisfying (15) gives the expression of current vector in the flux weakening region III as

$$I_d = -\frac{\lambda_m}{L_d}, \quad I_q = \frac{u_{\text{lim}}}{\omega_e L_q}. \tag{17}$$

The output characteristics versus speed of the both motors are calculated and shown in Figs. 16 and 17, respectively. From Fig. 16(a) and (b) and Fig. 17(a) and (b), it can be seen that both motors have the advantage of wide speed range, which benefit from their inherently large *d*-axis inductances. At base speed and nominal current, the output torque and power of the ISDW motor is 1.31 times higher than that of the FSCW one. Therefore, the ISDW motor can offer much higher torque than the FSCW one. Figs. 16(c) and 17(c) show the terminal voltage versus speed of the both motors. It can be found that the limits of terminal voltage of the FSCW and ISDW motors are 100 and 264 V_{pk}, respectively. It means that although the ISDW motor can offer high torque and output power, it also demands an inverter with greater capacity at the same time. The current and current phase angle versus speed of the both motors are shown in Fig. 16(d) and (e) and Fig. 17(d) and (e), respectively, which are consistent with the aforementioned analysis. The losses distributions and efficiency of the both motors are shown in Fig. 16(f) and (g) and Fig. 17(f) and (g), respectively. It can be observed that the FSCW motor takes the advantage of lower copper loss at

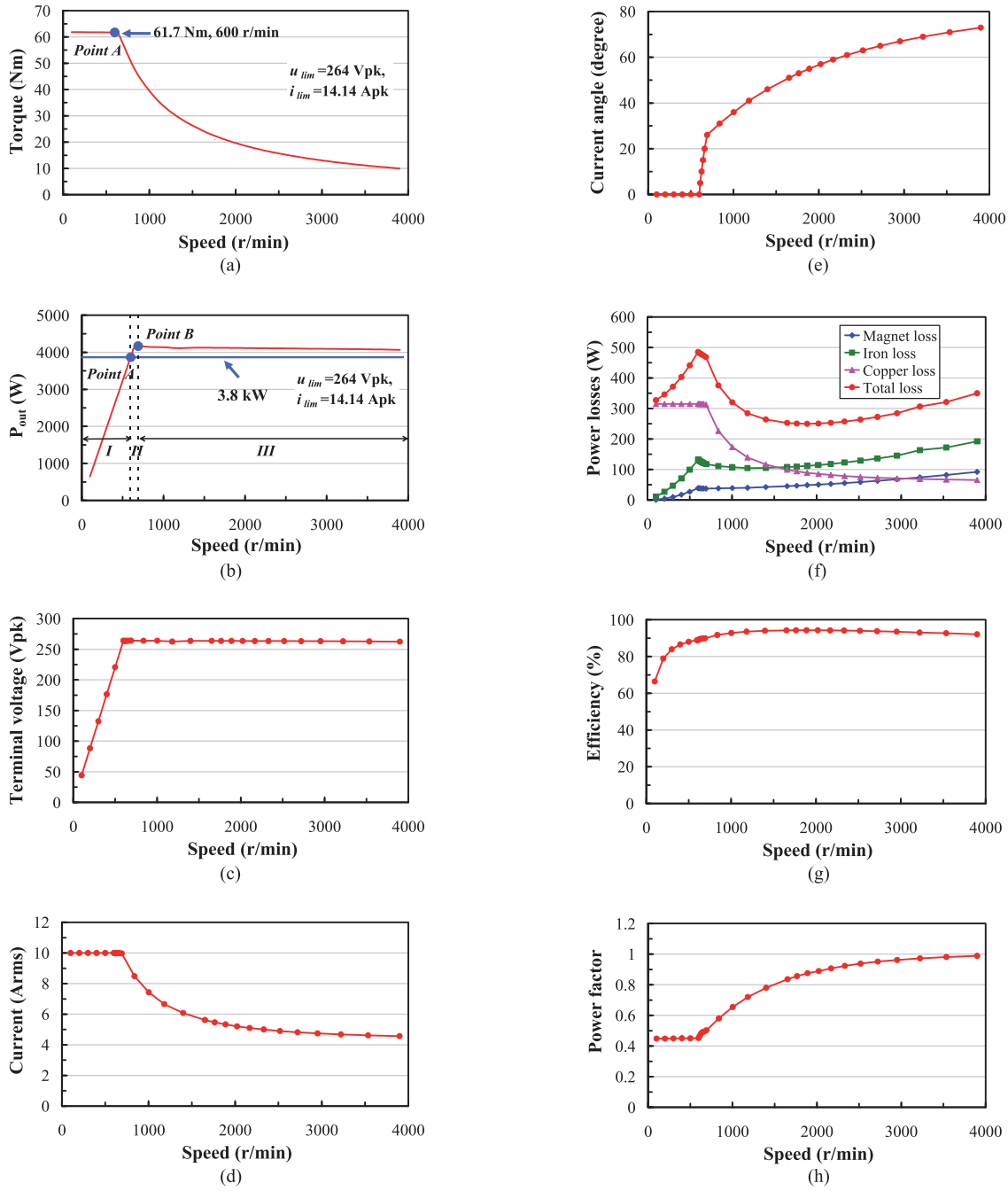

Fig. 17. Calculated output versus speed envelope for the ISDW motor. (a) Torque. (b) Output power. (c) Terminal voltage. (d) Current. (e) Current angle. (f) Power losses. (g) Efficiency. (h) Power factor.

the same current due to its reduced end length of winding and resistance, whereas it suffers from very high iron loss at high speed due to its lower armature winding pole pairs as compared with the ISDW motor. Therefore, the efficiency of the FSCW motor is inferior to that of the ISDW one as shown in Figs. 16(g) and 17(g). The power factors versus speed of both motors are shown in Figs. 16(h) and 17(h). It can be seen that both motors suffer from poor power factor at low speed, while power factor significantly enhance with the speed.

Table IV shows a quantitative comparison of the FSCW and ISDW PMV motors at low speed of 600 r/min and high speed of 3000 r/min. The maximum torque and output power of the ISDW motor are 2.31 and 2.66 times that of the FSCW one. Also, an inverter with much higher capacity should be employed for the ISDW motor since it has much higher apparent power than that of the FSCW motor. The FSCW motor takes the merits of lower total mass and copper usage due to the employment of concentrated winding layout. The efficiency of the ISDW motor is slightly higher than that of the FSCW one at low speed, while at the high speed of 3000 r/min the efficiency of the ISDW motor is much higher than that of the FSCW one due to its much lower iron loss.

TABLE IV
QUANTITATIVE COMPARISON OF THE FSCW AND ISDW PMV MOTORS

Items	FSCW		ISDW	
Outside rotor radius, R_{ro} (mm)	70		70	
Stack length, l_{stk} (mm)	60		60	
Winding type	Concentrated		Distributed	
Copper mass (kg)	1.09		2.21	
Magnet mass (kg)	0.61		0.37	
Iron mass (kg)	3.54		3.94	
Total mass (kg)	5.24		6.52	
Motor volume (L)	0.92		0.92	
Slot fill factor	0.5		0.5	
Maximum stator voltage (V_{rms})	75		190	
Maximum stator current (A_{rms})	10		10	
Maximum apparent power (kV·A)	3.50		9.30	
Maximum output power (kW)	1.95		4.17	
Rational speed (r/min)	600	3000	600	3000
Maximum torque (N·m)	26.7	–	61.7	–
Maximum torque per motor mass (N·m/kg)	5.1	–	9.5	–
Maximum torque per motor volume (N·m/L)	29.0	–	67.2	–
Efficiency (%)	87.1	75.8	88.9	93.2
Copper loss	155	60	315	72
Iron loss	82	400	130	148
Magnet loss	12	100	39	68
Current (A_{rms})	10	5.7	10	4.7
Current density (A_{rms}/mm^2)	6.6	3.8	6.6	3.1

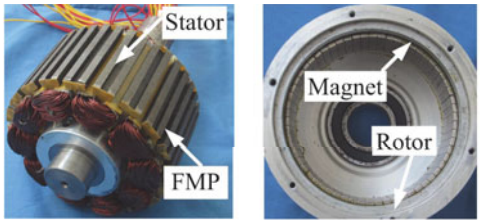

(a) (a)

Fig. 18. Prototype motor. (a) Stator. (b) Rotor.

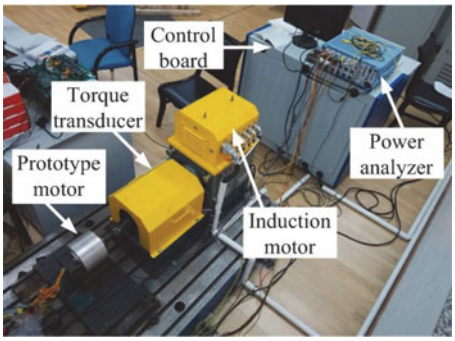

Fig. 19. Experimental setup.

VI. EXPERIMENTAL RESULTS

In order to experimentally validate the theoretical analysis, the PMV motor with FSCW has been built as shown in Fig. 18. The performance tests of the prototype motor are conducted on an induction dynamometer as shown in Fig. 19, in which the experiments refer to the room temperature of the motor and the magnets of 70 °C. The experimental results of the four-phase no-load back-EMF waveforms at the speed of 600 r/min are shown in Fig. 20, in which e_a, e_b, e_c, and e_d represent the

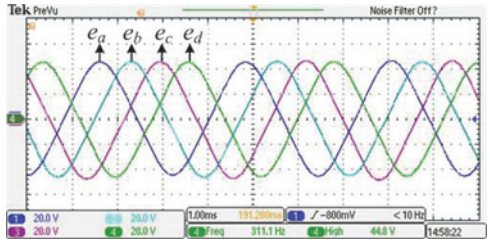

Fig. 20. Experimental results of the no-load phase back-EMFs (20 V/div, 1 ms/div).

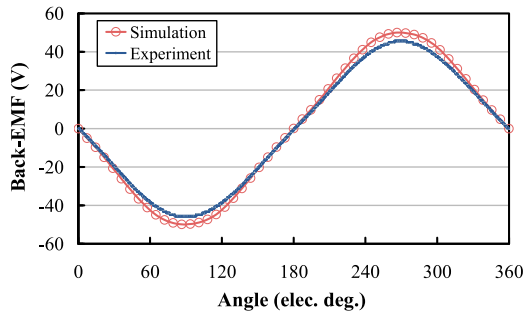

(a)

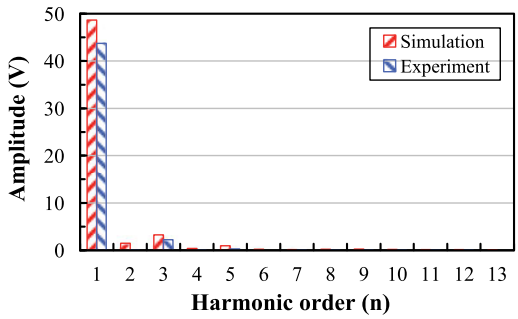

(b)

Fig. 21. Comparison of the experimental and simulated phase back-EMFs. (a) Waveforms. (b) Harmonic analysis.

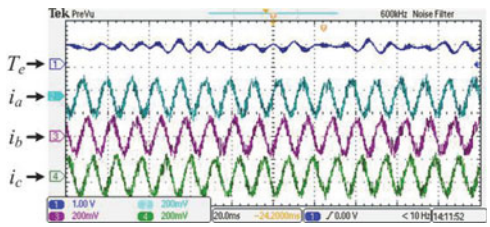

Fig. 22. Experimental torque and current waveforms (4 N·m/div, 2 A/div, 20 ms/div).

back-EMF waveforms of phase A, phase B, phase C, and phase D, respectively. The comparisons of experimental and simulated results of the back-EMF waveforms and corresponding harmonic analysis are shown in Fig. 21. It can be seen that the measured fundamental component is about 8% lower than the simulated one which is mainly due to the effect of lamination factor, end effect, and manufacturing error. The total harmonic distortion of the simulated and measured results in the FSCW motor are 7.8% and 4.3%, respectively. Fig. 22 shows the torque (T_e) and current waveforms under $i_d = 0$ control, in which i_a,

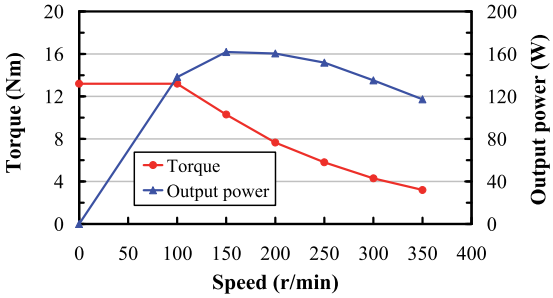

Fig. 23. Experimental torque and output power versus speed.

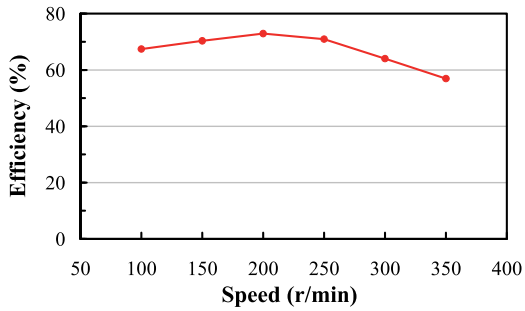

Fig. 24. Experimental efficiency versus speed.

i_b, and i_c represent the current waveforms of phase A, phase B, and phase C, respectively. It is noticed that the measured torque ripples is larger than the simulated ones. This is due to the fact that simulated torque waveforms only take into account the ripple resulted from electromagnetic force, while the operating, practical, and manufacturing torque ripples are neglected.

By using the *LCR* meter, the inductance of the prototype motor can be measured. The average value of the simulated self-inductance is 3.16 mH, which is slightly smaller than that of the experimental one with 3.21 mH. Nevertheless, the simulated results agree with the experimental results in principle; hence, to provide partial support for the flux weakening analysis of the PMV motors. In addition, it is worthwhile to note that the measured average mutual inductance is very small, which can be neglected as compared with the self-inductance. Thus, it verifies the FSCW PMV motor can offer desirable fault tolerant capability [4], [18], [26].

Flux weakening capability of the FSCW and ISDW PMV motors are first verified by light load test on the prototype FSCW motor. Fig. 23 shows the experimental results of the torque and output power versus speed at voltage and current limits of 27 V_{pk} and 6 A_{rms}. It can be seen that speed of the FSCW motor can be extended with flux weakening operation. Also, its output power can be increased by utilizing the maximum power control strategy, which partially validates the aforementioned theoretical analysis. The experimental efficiency of the prototype motor is shown in Fig. 24. The efficiency at the corner speed of 100 r/min is only about 68%, whereas its maximum efficiency is only about 72%, which occurs at the speed of 200 r/min. The experimental results illustrate the efficiency of the prototype motor is low. Nevertheless, the low efficiency is credible and reasonable because the motor operates at light load, in which its copper loss is very prominent as compared with other losses and hence significantly reducing the efficiency. The ISDW PMV motor is being fabricated and the nominal torque and power tests for the both motors will be carried on in the future.

VII. Conclusion

In this paper, two five-phase PMV motors with FSCW and ISDW have been presented and analyzed, respectively. The validity of theoretical analysis of the two motors has been verified by simulations. Furthermore, the FSCW PMV motor has been prototyped and tested. The experimental results provide partial support for theoretical analysis. Utilizing the well-known magnetic gearing effect both of them can output a high torque at low speed, which is attractive for direct-drive applications. The comparative studies on the two motors also show that the ISDW motor can offer much higher torque than the FSCW one. This is because that the ISDW one has greater slots per pole per phase, which can increase the modulation ratio of magnetic gearing effect. Although the output torque capability of the FSCW motor is relatively lower than that of the ISDW one, the FSCW one has the merit of reduced copper usage and the consequential reduction in copper loss. In addition, the FSCW one can be an excellent choice from the point of high reliability and fault tolerance. Hence, taking into account the special requirements, such as torque density and fault tolerance in some applications, motor designers should be careful to select appropriate winding layout and slots per pole per phase for PMV motors. When flux weakening strategy is employed, the simulated and experimental results show that both PMV motors can operate over a wide speed range. Therefore, it can be concluded that both of the FSCW and ISDW PMV motors have a bright future in direct-drive applications. At last, it is worth to mention that these findings in this paper also can be easily extended and employed for the conventional three-phase PMV motor designs.

References

[1] R. Wrobel and P. H. Mellor, "Design considerations of a direct drive brushless machine with concentrated windings," *IEEE Trans. Energy Convers.*, vol. 23, no. 1, pp. 319–328, Jun. 2008.

[2] S. Chung, J. Kim, Y. Chun, B. Woo, and D. Hong, "Fractional slot concentrated winding PMSM with consequent pole rotor for a low-speed direct drive: Reduction of rare-earth permanent magnet," *IEEE Trans. Energy Convers.*, vol. 30, no. 1, pp. 103–109, Mar. 2015.

[3] L. Jian and K. T. Chau, "A coaxial magnetic gear with halbach permanent-magnet arrays," *IEEE Trans. Energy Convers.*, vol. 25, no. 2, pp. 319–328, Jun. 2010.

[4] G. Liu, J. Yang, W. Zhao, J. Ji, Q. Chen, and W. Gong, "Design and analysis of a new fault-tolerant permanent-magnet vernier machine for electric vehicles," *IEEE Trans. Magn.*, vol. 48, no. 11, pp. 4176–4179, Nov. 2012.

[5] H. Yang, H. Lin, Z. Q. Zhu, S. Fang, and Y. Huang, "Novel flux-regulatable dual-magnet vernier memory machines for electric vehicle propulsion," *IEEE Trans. Appl. Supercond.*, vol. 24, no. 5, pp. 0601205-1–0601205-5, May 2014.

[6] Y. Guo, R. Qu, J. Li, Z. Zhu, and D. Li, "HTS vernier machine for direct-drive wind power generation," *IEEE Trans. Appl. Supercond.*, vol. 24, no. 5, pp. 5202905-1–5202905-5, May 2014.

[7] J. Li, K. T. Chau, J. Z. Jiang, C. Liu, and W. Li, "A new efficient permanent-magnet vernier machine for wind power generation," *IEEE Trans. Magn.*, vol. 45, no. 6, pp. 1475–1478, Jun. 2010.

[8] A. Ishizaki, T. Tanaka, K. Takasaki, and S. Nishikata, "Theory and optimum design of PM vernier motor," in *Proc. 7th Int. Conf. Elect. Mach. Drives*, Sep. 1995, pp. 208–212.
[9] A. Toba and T. A. Lipo, "Generic torque-maximizing design methodology of surface permanent-magnet vernier machine," *IEEE Trans. Ind. Appl.*, vol. 36, no. 6, pp. 1539–1546, Nov./Dec. 2000.
[10] X. Li, K. T. Chau, and M. Cheng, "Comparative analysis and experimental verification of an effective permanent-magnet vernier machine," *IEEE Trans. Mag.*, doi: 10.1109/TMAG.2014.2359853
[11] D. Li, R. Qu, and T. A. Lipo, "High power factor vernier permanent magnet machines," *IEEE Trans. Ind. Appl.*, vol. 50, no. 6, pp. 3664–3674, Nov./Dec. 2014.
[12] D. G. Dorrell, A. M. Knight, L. Evans, and M. Popescu, "Analysis and design techniques applied to hybrid vehicle drive machines—Assessment of alternative IPM and induction motor topologies," *IEEE Trans. Ind. Electron.*, vol. 59, no. 10, pp. 3690–3699, Oct. 2012.
[13] I. Boldea, L. N. Tutelea, L. Parsa, and D. G. Dorrell, "Automotive electric propulsion systems with reduced or no permanent magnets: An overview," *IEEE Trans. Ind. Electron.*, vol. 61, no. 10, pp. 5696–5711, Nov. 2014.
[14] A. Chiba, K. Kiyota, N. Hoshi, M. Takemoto, and S. Ogasawara, "Development of a rare-earth-free SR motor with high torque density for hybrid vehicles," *IEEE Trans. Energy Convers.*, vol. 30, no. 1, pp. 175–182, Mar. 2015.
[15] Q. Chen, G. Liu, W. Zhao, M. Shao, and Z. Liu, "Design and analysis of the new high reliability motors with hybrid permanent magnet material," *IEEE Trans. Magn.*, vol. 50, no. 12, pp. 8207010-1–8207010-10, Dec. 2014.
[16] R. Hosoya, H. Shimada, and S. Shimomura, "Design of a ferrite magnet vernier machine for an in-wheel machine," in *Proc. IEEE Energy Convers. Congr. Expo.*, 2011, pp. 2790–2797.
[17] S. Chung, J. Kim, B. Woo, D. Hong, J. Lee, and D. Koo, "A novel design of modular three-phase permanent magnet vernier machine with consequent pole rotor," *IEEE Trans. Magn.*, vol. 47, no. 10, pp. 4215–4218, Oct. 2011.
[18] A. M. EL-Refaie, "Fractional-slot concentrated-windings synchronous permanent magnet machines: Opportunities and challenges," *IEEE Trans. Ind. Electron.*, vol. 57, no. 1, pp. 107–121, Jan. 2010.
[19] L. Alberti, M. Barcaro, and N. Bianchi, "Design of a low torque ripple fractional-slot interior permanent magnet motor," *IEEE Trans. Ind. Appl.*, vol. 50, no. 3, pp. 1801–1808, May/Jun. 2014.
[20] W. Zhao, M. Cheng, K. T. Chau, R. Cao, and J. Ji, "Remedial injected-harmonic-current operation of redundant flux-switching permanent-magnet motor drives," *IEEE Trans. Ind. Electron.*, vol. 60, no. 1, pp. 151–159, Jan. 2013.
[21] K. Okada, N. Niguchi, and K. Hirata, "Analysis of a vernier motor with concentrated windings," *IEEE Trans. Magn.*, vol. 49, no. 5, pp. 2241–2244, May 2013.
[22] J. Yang, G. Liu, W. Zhao, Q. Chen, Y. Jiang, L. Sun, and X. Zhu, "Quantitative comparison for fractional-slot concentrated-winding configurations of permanent-magnet vernier machines," *IEEE Trans. Magn.*, vol. 49, no. 7, pp. 3826–3829, Jul. 2013.
[23] W. Guo and C. Zhang, "Design and control of a high torque density and high field-weakening performance permanent magnet vernier machine," in *Proc. IEEE Int. Conf. Elect. Mach. Syst.*, 2010, pp. 1077–1082.
[24] A. M. El-Refaie and T. M. Jahns, "Optimal flux weakening in surface PM machines using fractional slot concentrated windings," *IEEE Trans. Ind. Appl.*, vol. 41, no. 3, pp. 790–800, May/Jun. 2005.
[25] A. M. El-Refaie and T. M. Jahns, "Analysis of surface permanent magnet machines equipped with concentrated windings," *IEEE Trans. Energy Convers.*, vol. 21, no. 1, pp. 34–43, Mar. 2006.
[26] Q. Chen, G. Liu, W. Zhao, L. Sun, M. Shao, and Z. Liu, "Design and comparison of two fault-tolerant interior-permanent-magnet motors," *IEEE Trans. Ind. Electron.*, vol. 61, no. 12, pp. 6615–6623, Dec. 2014.
[27] L. Jian, G. Xu, C. C. Mi, K. T. Chau, and C. C. Chan, "Analytical method for magnetic field calculation in a low-speed permanent-magnet harmonic machine," *IEEE Trans. Energy Convers.*, vol. 26, no. 3, pp. 862–870, Sep. 2011.
[28] B. Kim and T. A. Lipo, "Operation and design principles of a PM vernier motor," *IEEE Trans. Ind. Appl.*, vol. 50, no. 6, pp. 3656–3663, Nov./Dec. 2014.
[29] W. L. Soong and T. J. E. Miller, "Field-weakening performance of brushless synchronous ac motor drives," *IEE Proc. Elect. Power Appl.*, vol. 141, no. 6, pp. 331–340, Nov. 1994.

Liang Xu (S'15) received the B.Sc. degree in electrical engineering and automation from Soochow University, Suzhou, China, in 2011, and the M.Sc. degree in power electronics and power drives from Jiangsu University, Zhenjiang, China, in 2014, where he is currently working toward the Ph.D. degree.

His research interests include electrical machines and drives.

Guohai Liu (M'07) received the B.Sc. degree from Jiangsu University, Zhenjiang, China, in 1985, and the M.Sc. and Ph.D. degrees from Southeast University, Nanjing, China, in 1988 and 2002, respectively, in electrical engineering and control engineering.

Since 1988, he has been with Jiangsu University, where he is currently a Professor and the Dean of the School of Electrical Information Engineering. He has authored or coauthored more than 150 technical papers, four textbooks, and holds 15 patents in these areas. His teaching and research interests include electrical machines, motor drives for electric vehicles, and intelligent control.

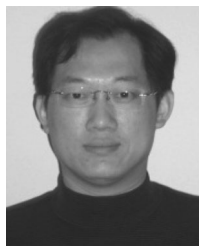

Wenxiang Zhao (M'08–SM'14) received the B.Sc. and M.Sc. degrees in electrical engineering from Jiangsu University, Zhenjiang, China, in 1999 and 2003, respectively, and the Ph.D. degree in electrical engineering from Southeast University, Nanjing, China, in 2010.

From 2008 to 2009, he was a Research Assistant with the Department of Electrical and Electronic Engineering, University of Hong Kong, Hong Kong. From 2013 to 2014, he was a Visiting Professor with the Department of Electronic and Electrical Engineering, University of Sheffield, Sheffield, U.K. He has been with Jiangsu University since 2003, where he is currently a Professor with the School of Electrical Information Engineering. His current research interests include electric machine design, modeling, fault analysis, and intelligent control. He has authored and coauthored more than 130 technical papers in these areas.

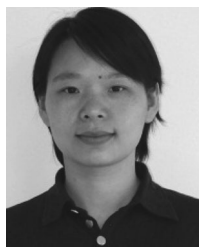

Jinghua Ji received the B.Sc., M.Sc., and Ph.D. degrees in electrical engineering from Jiangsu University, Zhenjiang, China, in 2000, 2003, and 2009, respectively.

She has been with the School of Electrical Information Engineering, Jiangsu University, since 2000, where she is currently an Associate Professor. Her research interests include motor design and electromagnetic field computation.

Huawei Zhou received the B.Sc. and M.Sc. degrees in control engineering from Jiangsu University, Zhenjiang, China, in 2003 and 2006, respectively, and the Ph.D. degree in electrical engineering from the Graduate University of the Chinese Academy of Sciences, Beijing, China, in 2012.

Since 2003, he has been with Jiangsu University, where he is currently an Associate Professor with the School of Electrical Information Engineering. His teaching and research interests include electric machine modeling, fault-tolerance analysis, and intelligent control.

Wanxiang Zhao received the B.Sc. degree in electrical engineering from Jiangsu University, Zhenjiang, China, in 2013, where he is currently working toward the M.Sc. degree in control engineering.

His research interests include electrical machines, motor drives for electric vehicles, and intelligent control.

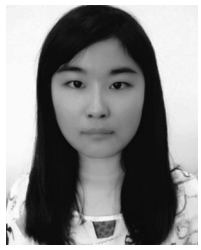

Tingting Jiang received the B.Sc. degree in mechanical engineering and automation from the Huaiyin Institute of Technology, Huaian, China, in 2012. She is currently working toward the M.Sc. degree in electrical engineering at Jiangsu University, Zhenjiang, China.

Her research interests include the computation of electromagnetic loss and thermal analysis for permanent-magnet machine.